AgriEngineering

Article

Modeling Sugar Cane Evapotranspiration Using UAV Thermal and Multispectral Images in Northeast Brazil

Marcos Elias de Oliveira, Júnior [1], Alexandre Ferreira do Nascimento [2,*], Ericka Aguiar Carneiro [2], Guillaume Francis Bertrand [1,3], Lúcio André de Castro Jorge [4], Érick Rúbens Oliveira Cobalchini [5], Edson Wendland [5], Valéria Peixoto Borges [2] and Davi de Carvalho Diniz Melo [1,*]

1 Department of Civil and Environmental Engineering, Federal University of Paraíba, Campus I, João Pessoa 58051-900, PB, Brazil; marcos.pdfrn@gmail.com (M.E.d.O.J.)
2 Department of Soil and Rural Engineering, Federal University of Paraíba, Campus II, Areia 58397-000, PB, Brazil; ericka27aguiar@gmail.com (E.A.C.);valeria.borges@academico.ufpb.br (V.P.B.)
3 Chrono-Environment (UMR 6249), CNRS, Université Marie et Louis Pasteur, F-25200 Montbéliard, France
4 Embrapa Instrumentation, Brazilian Agricultural Research Corporation, São Carlos 13561-206, SP, Brazil; lucio.jorge@embrapa.br
5 Department of Hydraulics and Sanitation, São Carlos' School of Engineering, University of São Paulo, São Carlos 13566-590, SP, Brazil; cobalchini@usp.br (É.R.O.C.); ew@sc.usp.br (E.W.)
* Correspondence: alexandre_fdn@hotmail.com (A.F.d.N.); davi.diniz@academico.ufpb.br (D.d.C.D.M.)

Abstract

Understanding crop water use is essential for improving agricultural water management and ensuring sustainable food production, especially in regions with limited water resources. Evapotranspiration (ET) is a key component of the hydrological cycle, directly influencing irrigation planning and crop productivity. However, accurately estimating ET at local scales remains a challenge due to the limitations of conventional measurement methods and the difficulty of integrating high-resolution remote sensing data. This study investigates the estimation of terrestrial evapotranspiration (ET) in a sugarcane cultivation area located in the northern coastal region of Paraíba, Brazil, using meteorological data and aerial images acquired by an Unmanned Aerial Vehicle (UAV). We adapted the PT-JPL model to estimate ET at the local scale, using thermal and multispectral imagery obtained from UAVs. Data validation was performed using surface energy balance measurements obtained from a micrometeorological tower, thereby enabling comparison of estimated and observed ET values. The results demonstrated strong correlations between modeled predictions and field measurements of net radiation (R^2 = 0.85), with performance metrics indicating moderate reliability for local-scale simulated ET when compared to flux-tower-based ET (R^2 = 0.48; RMSE ≈ 0.045 mm/30 min). This research highlights the potential of integrating UAV-based remote sensing with the PT-JPL model to improve understanding of crop water use, support irrigation management, and contribute to sustainable agricultural practices.

Keywords: surface temperature; energy balance; crop monitoring

Academic Editor: Leonardo Conti

Received: 5 February 2026
Revised: 24 March 2026
Accepted: 27 March 2026
Published: 9 April 2026

1. Introduction

Understanding hydrological processes is essential for the efficient management of water resources [1], especially in a global context of climate change, with an increase in the occurrence of natural disasters related to extreme events [2], while crop water demand continues to grow. Among the various components of the hydrological cycle, precipitation

and evapotranspiration (ET) represent major inputs and outputs, respectively, in the water balance [3].

ET encompasses both the evaporation of water from the surface and the transpiration from plants and is a key process for maintaining the water and energy balance at Earth's surface. Monitoring ET is crucial for any agricultural practice, as it directly affects crop water requirements and irrigation planning. However, unlike precipitation, evapotranspiration is not easily measured. Lysimeter measurements or empirical methods have their own challenges and limitations [4,5]. Lysimeters are expensive to construct, install, and maintain [6–8]. Moreover, the loss of soil integrity during installation may compromise the representativeness of point-scale measurements at larger scales [9]. Empirical methods are site-specific, depending on local weather conditions, and may require a large number of input parameters [10–13]. Some of these parameters are not always measured at meteorological stations [10,14].

Flux towers provide the most accurate method for measuring ET as they directly measure water vapor flux; however, the eddy covariance method has significant limitations in spatial representativeness. Measurements are confined to a specific area of influence (footprint), which may not represent larger regions, particularly in heterogeneous landscapes. Furthermore, the footprint area varies with meteorological conditions—particularly wind direction and speed—which can introduce variability into the data and hinder extrapolation to larger spatial scales [15–18]. Precise evapotranspiration (ET) simulations are fundamental for modeling hydrological processes, crop development, and ecosystem water-use efficiency [19].

In recent decades, remote sensing technology has emerged as a promising tool for estimating ET. The development of various algorithms [20] that use reflectance and thermal spectrum data has contributed to this progress. One such example is the PT-JPL model (Priestley–Taylor Jet Propulsion Laboratory), a satellite-based model used to estimate ET at regional and global scales. The PT-JPL model calculates ET separately for vegetation (transpiration and evaporation of water intercepted by the canopy) and soil, using a combination of satellite parameters (surface temperature and vegetation indices) and meteorological conditions. It employs an adaptation of the Priestley and Taylor equation to estimate actual ET (ETa) from potential ET (ETp) [21]. However, most satellite sensors can only provide useful ET data under clear-sky conditions [22].

In Northeast Brazil, sugarcane (*Saccharum officinarum*) is one of the most economically important crops [23]. Sugarcane is a water-intensive crop [24], making accurate estimation of ET essential for efficient irrigation management and sustainable water resource use. However, this region often experiences frequent cloud cover [25], which limits the availability of satellite-based ET data. Consequently, alternative monitoring approaches, such as aerial imagery obtained from remotely piloted aircraft (RPA), are particularly relevant for sugarcane fields in northeastern Brazil, enabling precise and timely estimation of crop water demand.

RPA-based data applications include monitoring crop disease symptoms and diseases [14], crop height monitoring [26], and crop ET estimation [27,28]. Despite these advances, acquiring and processing RPA imagery remains time-consuming and costly. Therefore, users seeking to streamline the procedure may adopt open-source tools or software for ET modeling.

Despite significant progress, several challenges remain unresolved in the study of terrestrial ET. These include accurate partitioning of ET among soil evaporation, canopy interception, and plant transpiration; representation of irrigation and agricultural management in models; the influence of spatial heterogeneity in soil, vegetation, and topography; and the interactions among radiation, soil moisture, and vegetation responses under wa-

ter stress. Furthermore, reconciling ground-based measurements with remote-sensing estimates across multiple spatial and temporal scales remains challenging [29,30].

The QWaterModel and PT-JPL were selected for this study because of their complementary approaches to estimating surface energy fluxes: QWaterModel is physically based and relies primarily on surface temperature, whereas PT-JPL integrates remote-sensing data with vegetation and meteorological parameters. Comparing both models provides an opportunity to evaluate their relative performance and applicability in tropical agricultural conditions. In this context, it is essential to understand how such free tools can be effectively integrated with evapotranspiration models to accurately estimate ET. Like this, the present study aims to map ET using meteorological data and aerial imagery obtained via RPA.

2. Materials and Methods

2.1. Study Area

A sugarcane crop field (5.14 ha) was the subject of this study. It is located in Rio Tinto (6°53′5.65″ S, 35°2′5.46″ W), a municipality on the northern coast of Paraíba state (Figure 1), in Northeast Brazil.

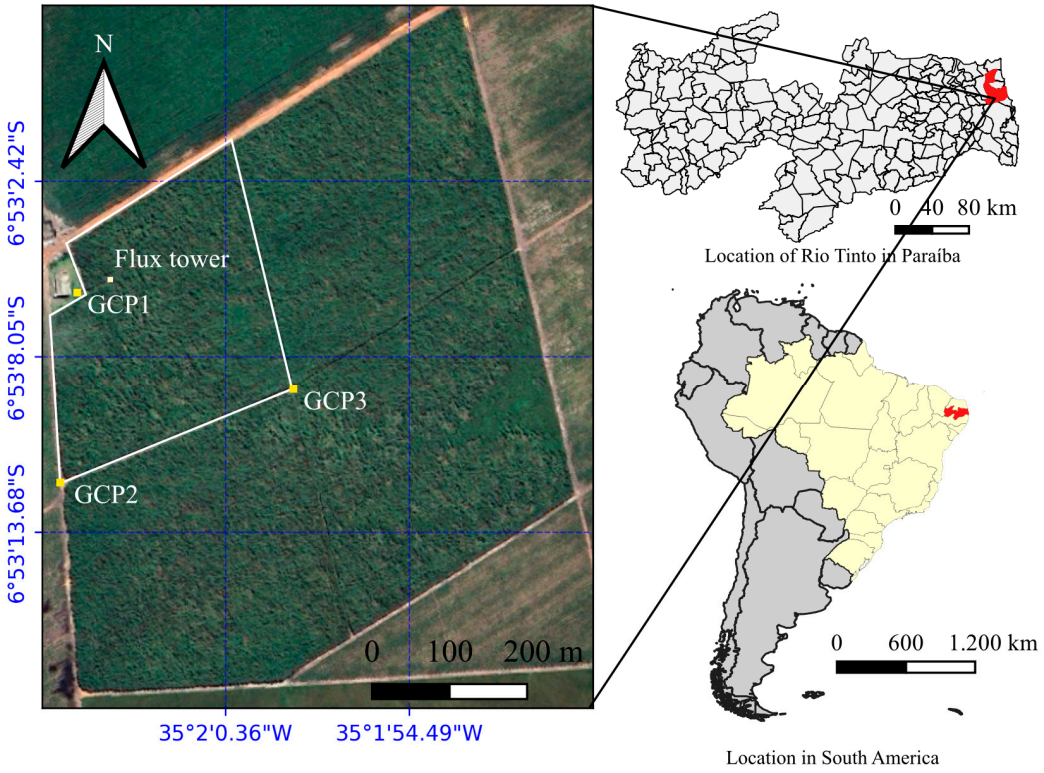

Figure 1. Study area: sugar cane planting (5.14 ha) located within the Rio Tinto Municipality, Paraíba state. The white dot indicates the location of the flux tower that provided the micrometeorological data for the analyzed period (October 2022–August 2023); the yellow dots indicate the position of the ground control points (GCPs) used for georeferencing.

Rio Tinto has a humid tropical climate of the As type, with annual rainfall of 1423 mm. The rainy season occurs from March to August, with a notable peak in June [31].

The monthly mean temperatures, determined from the station of the Brazilian National Institute of Meteorology (INMET) in Camaratuba (6°33′42.7″ S, 35°08′07.1″ W), the closest to Rio Tinto (37 km) (period from 1999 to 2020), range between 24 and 27 °C, as shown in Figure 2.

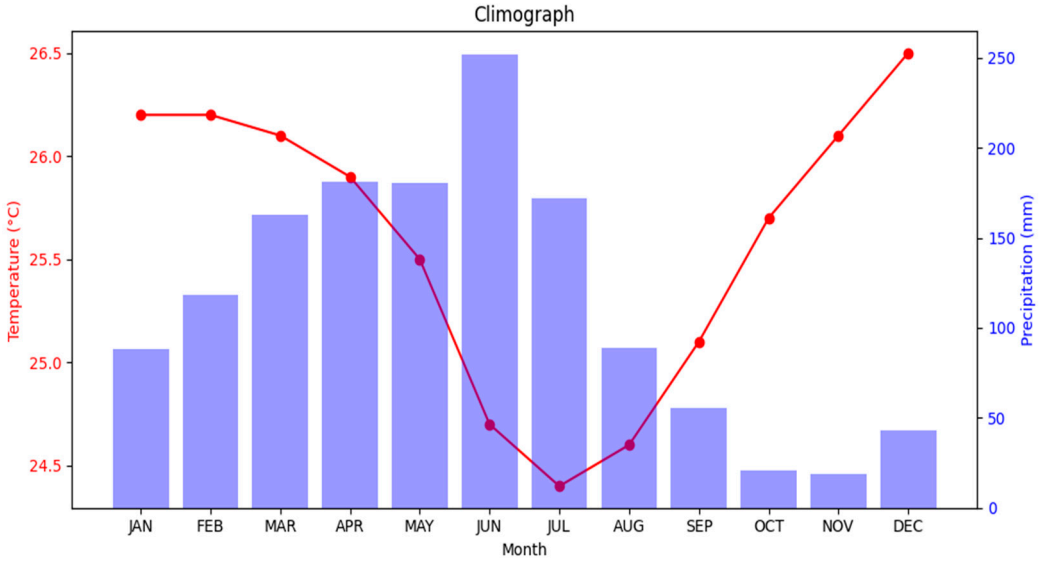

Figure 2. Climatology of the municipality of Rio Tinto.

The crop irrigation is done using a subsurface drip irrigation system, in which water is applied directly to the root zone of the plants via hoses buried 20 cm below the surface, with a flow rate of 0.6 L/h. Irrigation was performed daily, reaching a cumulative monthly application of 80 mm, with a set duration and scheduled time, usually after 16:00 PM.

Aerial thermal images were collected using the DJI Mavic 2 Enterprise Advanced, equipped with a thermal camera (spectral channel 8–14 µm) with a 640 × 512 sensor resolution. Multispectral images were collected using the DJI Phantom 4 equipped with a six-camera array, including one RGB and five monochromatic sensors (Blue, Green, Red, Red Edge, and Near-Infrared), each with a 1.2 MP (1600 × 1300 pixels) resolution. The image acquisition campaign (Table 1) followed a bi-monthly frequency, which was the highest possible cadence given the logistical and funding parameters of the study. Flight times were primarily centered around midday to mitigate the impact of shadows on the multispectral data, although slight variations occurred due to the time of arrival at the experimental site and field staff scheduling. The meteorological conditions during the flights were stable, with little variability in the air temperature and relative humidity, no precipitation, and high solar radiation (Table 1).

Table 1. Weather conditions during UAV imaging.

Date/Time UTC-3	Air Temperature (°C)	Air Relative Humidity (%)	Precipitation (mm)	Net Radiation (W/m^2)	Shortwave Radiation (W/m^2)
11 October 2022 12:00	28.4	52.8	0.0	413.8	749.3
4 November 2022 12:00	28.6	57.1	0.0	386.8	731.4
16 November 2022 09:00	27.6	61.3	0.0	461.7	772.7
25 November 2022 08:30	27.9	62	0.0	367.7	710.5
22 December 2022 14:30	28.5	57.8	0.0	355.1	523.2
24 March 2023 10:30	27.3	72.1	0.0	380.2	551.1
28 April 2023 15:00	30.2	52.5	0.0	346.1	519.8
26 May 2023 13:00	30.1	52.0	0.0	616.7	900
21 July 2023 12:30	29	63.7	0.0	568.9	840
18 August 2023 08:30	24.6	79.3	0.0	307.5	665.2

The flight was conducted at an altitude of 80 m above ground to balance operational feasibility and thermal resolution. Combined with a lateral and frontal overlap rate of 70% and 80%, respectively, such a configuration provided sufficient spatial coverage and radiometric precision for comparative temperature analysis across the study area. Additionally, three ground control points (GCP, Figure 1) were defined and georeferenced using a high-precision Global Navigation Satellite System receiver in real-time kinematic (RTK) mode. These points were placed on the ground to appear in visible locations in the photographs, thereby facilitating their identification during image processing [32].

2.2. Field Data Acquisition and Analysis of Thermal Images

We used an ST-620 handheld pyrometer (Incoterm, Porto Alegre, Brazil) to support thermal calibration. We used at least three ground control points, as suggested by [33] and the Pix4DMapper software (version 4.9.0), to process the thermal and multispectral images. The number of points was determined based on the observed high linearity of the thermal sensor response (see Results section), enabling a reliable radiometric correction even with a streamlined sampling design. To improve the accuracy of the results, we performed geometric correction of the images, including both image alignment and correction of geometric distortions. The output of this stage is an orthomosaic of digital numbers (DN) representing the radiometric surface temperature.

Thermal radiometric temperature, represented by the DN, was converted to surface temperature using calibration equations, obtained by least-squares regression between pixel values and surface temperature measured in situ. Subsequently, these measurements were compared with the UAV-based surface temperature (Ts) provided by DJI Thermal Analysis software, version 2.1.

The following data are required to retrieve Ts: surface emissivity (0.95), air temperature, and the camera's flight height (distance from the ground), all at the time of image capture. Emissivity corrects the apparent temperature displayed by the camera. Atmospheric compensation, which distorts the radiation between the camera and the object, is performed using air temperature and flight altitude [34].

2.3. Ground-Truth Data

Ground-based meteorological data, from the flux tower (Figure 1) and shown in Table 1, were used to validate the UAV-based ET estimates. Energy balance components were measured at 30 min intervals, including Rn with an NR-Lite Net Radiometer (Kipp & Zonen, Delft, The Netherlands) and G with two Hukseflux HFP01 (Hukx Sensor Technology, Delf, The Netherlands) heat flux sensors (row spacing and inter-row spacing) at a depth of 5 cm. Soil temperature (107 probe, Campbell Scientific, Logan, UT, USA) and soil moisture (Campbell Scientific CS616) sensors were applied to correct the heat flux measurements to surface heat flux. Sensible heat flux (H) was calculated using the eddy-covariance method. The collection and storage of data measurements was conducted using a CR1000X Campbell Scientific datalogger.

$$H = \rho \times c_\rho \times \overline{w \times T_{so}} \quad (1)$$

where ρ is the air density ($\frac{\text{kg}}{\text{m}^3}$), c_ρ is the specific heat of air ($\frac{\text{J}}{\text{kg} \times \text{K}}$), $\overline{w}$ is the mean vertical wind speed (m/s) and T_{so} is the mean sonic temperature (K) [35]. T_{so} and $\overline{w}$ were determined using a Young Model 81000 sonic anemometer (R. M. Young Company, Traverse City, MI, USA). The sonic anemometer was programmed to record data at 10 Hz, storing the averages obtained for each variable every half hour. The measurement period spans from 1 October 2022 to 31 August 2023. Tower-based ET was, then, computed as the residual of the energy balance: $\lambda ET = Rn - G - H$, where $\boldsymbol{\lambda}$ is the latent heat of vaporization of water.

The QWater model was employed to map Rn and G across the entire area, based on UAV surface temperature maps. QWaterModel estimates ET based on the DATTUTDUT (Deriving Atmosphere Turbulent Transport Useful To Dummies Using Temperature) energy-balance model, using surface temperature maps as inputs and the image acquisition time in UTC [36].

To improve result accuracy, the plugin provides several additional options: minimum and maximum air temperatures, in Kelvin (K); shortwave and net radiation (W/m^2); and heat flux (W/m^2). The values for atmospheric transmissivity and emissivity are pre-filled and were obtained from [37]. These values can be modified depending on local conditions. Other optional but recommended parameters are latitude, longitude, and altitude. Finally, the user must specify the time period for calculating ET and, optionally, the instantaneous air temperature (K) at the moment the thermal image was taken [36].

As a result, the plugin generates a raster image in .tiff format with six bands:

- Band 1: Net radiation Rn (W/m^2);
- Band 2: Latent heat flux LE (W/m^2);
- Band 3: Sensible heat flux H (W/m^2);
- Band 4: Soil heat flux G (W/m^2);
- Band 5: Evaporative fraction EF (%);
- Band 6: Evapotranspiration ET (kg/time period).

Details of the input raster and statistical output results are stored in a .csv file [36].

According to [36], the QWater plugin is based on the energy balance model described by [37]. To compute Rn, the QWater applies Equation (2):

$$R_n = (1 - \alpha) \times R_S^{\downarrow} + \varepsilon_0 \times \varepsilon_a \times \sigma \times T_a^4 - \varepsilon_0 \times \sigma \times T_0^4 \quad (2)$$

where α is the surface albedo, ε_0 is the surface emissivity, ε_a is the atmospheric emissivity, σ is the Stefan–Boltzmann constant ($5.6697 \times 10^{-8} \frac{W}{m^2 \times K^4}$), T_0 is the surface temperature, and T_a is the air temperature. The G is estimated as a fraction of the net radiation. The α value depends on T_0 and the minimum (T_{min}) and maximum (T_{max}) surface temperatures of the thermal image and is calculated as follows:

$$\alpha = 0.05 + 0.02 \times \frac{T_0 - T_{mn}}{T_{mx} - T_{mn}} \quad (3)$$

ε_a, in turn, is calculated as follows:

$$\varepsilon_a = 1.08 \times \left(-ln(\tau)^{0.265}\right) \quad (4)$$

where τ is the atmospheric transmissivity, which depends on the solar zenith angle ϕ (in radians) and is mathematically defined by Equation (5):

$$\tau = 0.6 + 0.2 \times sen(\varphi) \quad (5)$$

For small areas, where the incident solar angle is nearly constant, it is assumed that $\tau = 0.7$ and $\varepsilon_a = 0.8$. Using τ and the exoatmospheric shortwave radiation (R_{s_exo}), which depends only on the Sun–Earth geometry, it is possible to calculate $R_S\downarrow$:

$$R_S^{\downarrow} = \tau \times R_{s\_exo} \quad (6)$$

The evaporative fraction (EF) quantifies the proportion of available radiation used for ET compared to the total amount of energy available at the Earth's surface. It is a measure

of the efficiency with which solar energy received by the surface is converted into ET [19,38]. Mathematically, it is expressed as follows:

$$EF = \frac{LE}{R_n - G} = \frac{LE}{LE + H} \quad (7)$$

High EF values indicate that a larger fraction of the available energy is used for evapotranspiration, suggesting a well-irrigated surface. Low EF values indicate that a larger fraction of the energy is used for heating the soil and atmosphere [37].

Net radiation is the most important component of the energy balance [39] and, therefore, carries more weight compared to the other components. Thus, we compared the Rn measured at the tower and the Rn estimated by the plugin within the field of view of the net radiometer, installed 5.85 m above ground with a half-angle of 75°. The field of view is circular, and using right triangle metric relations, a radius of r = 21.83 m was found (Figure 3). A shapefile from this area was generated to crop the sensor area for further comparisons and validations.

Figure 3. Net radiation sensor influence area, highlighted in orange.

Net radiation (Rn) and ground heat flux (G) maps for the crop area in days without flight were estimated using the flight-day map and flux tower data as references. In accordance with the recommendations and research results [40,41], the extrapolation was applied as follows: flight map × (Rn or G at flight time)/(Rn or G at the same time on the following day). This procedure allows the flight-day net radiation maps to be adjusted for temporal variations observed by the tower while maintaining the spatial coherence of the flight maps.

2.4. Priestley–Taylor Jet Propulsion Laboratory Model (PT-JPL) and Model Validation

PT-JPL is an evapotranspiration (ET) estimation model developed using vegetation indices derived from remote sensing data and meteorological data. The model employs the Priestley–Taylor (PT) algorithm, which quantifies ET based on potential evapotranspiration (PET) via latent heat flux [42]. The model requires five inputs: net radiation (Rn), Normalized Difference Vegetation Index (NDVI), Soil Adjusted Vegetation Index (SAVI), maximum air temperature, and vapor pressure [43].

Actual ET in the PT-JPL model is the sum of canopy transpiration (ETc), soil evaporation (ETs), and canopy interception evaporation (ETi), thus:

$$ET = ETc + ETs + ETi \quad (8)$$

The model predictive skill was assessed based on the analysis of scatter plots of measured versus modeled variables (Rn and ET), as well as through common metrics: coefficient of determination (R^2), mean squared error (MSE) and percent bias (PBIAS).

3. Results

3.1. Temperature Calibration Graphs and Thermal Maps

By cross-referencing pixel data from thermal images in DJI Thermal Analysis with corresponding pixels in processed orthomosaics, it was possible to obtain the conversion equations for Ts values with their respective scatter plots (Figure 4).

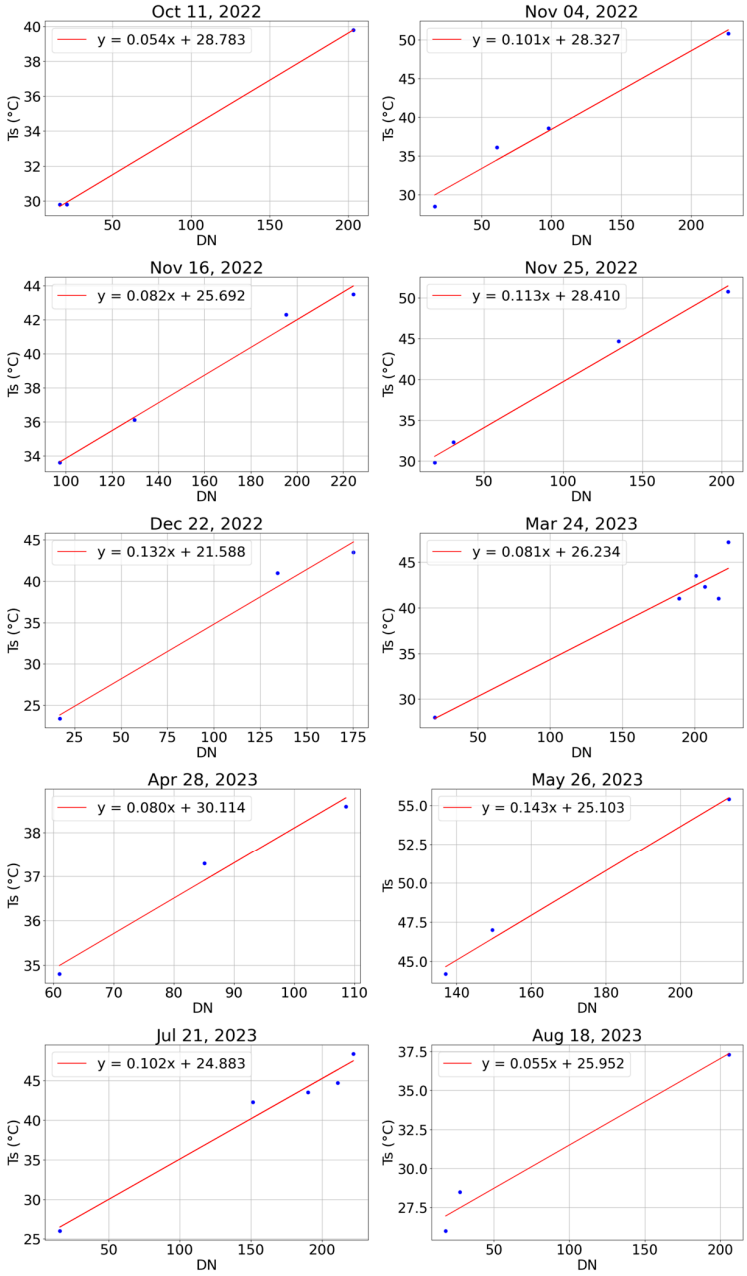

Figure 4. Relationship between digital number and surface temperature (°C).

The variations observed in the linear regression parameters (slope ranging from ~0.05 to ~0.14 and intercept from ~25 to ~30) are attributed to the dynamic nature of thermal remote sensing. The relationship between surface temperature and DN is influenced by atmospheric attenuation, air relative humidity and cloud cover. By applying flight-specific equations, we seek to compensate for these radiometric inconsistencies and achieve high precision in temperature estimation regardless of the specific environmental conditions at the time of overflight.

The thermal maps in Figure 5 and Figure S1 (Supplementary Materials) show that during the early stages of sugarcane cultivation, the surface temperature is much higher between the rows because they are directly exposed to sunlight. In more advanced stages, the surface temperature across the crop becomes relatively uniform.

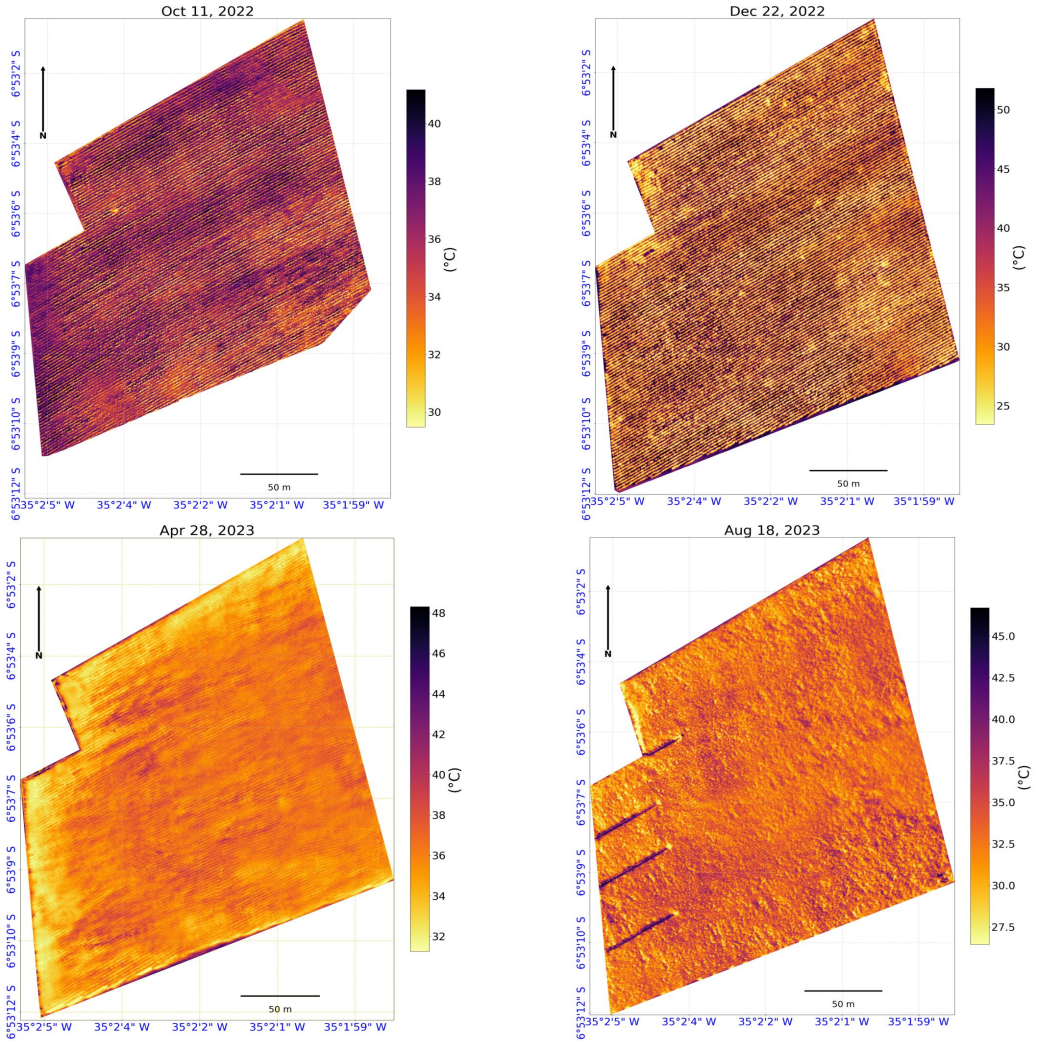

Figure 5. Surface temperature maps (°C).

3.2. Meteorological Conditions and Modeling with QWater Model

To evaluate the relationship between evapotranspiration and precipitation over the study period, Figure 6 presents the tower-based daily evapotranspiration (solid line) and precipitation (blue bars), allowing a clear visualization of the seasonal variations in these variables.

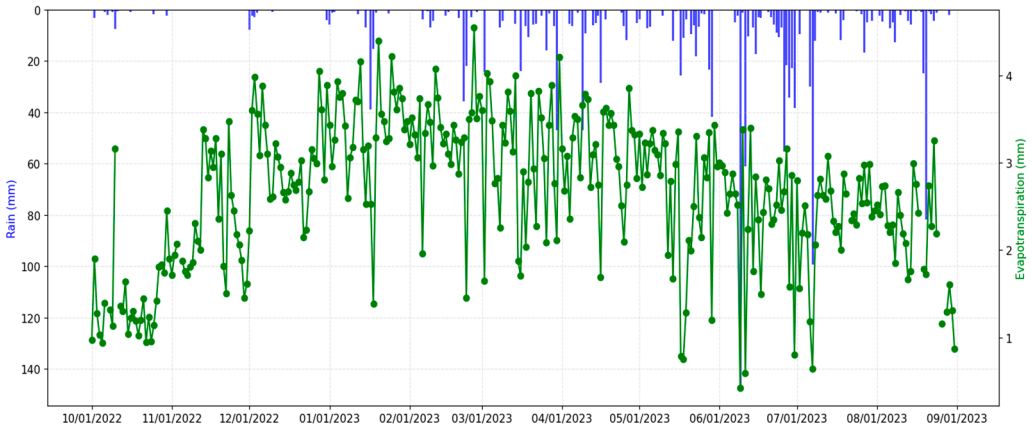

Figure 6. Evapotranspiration and precipitation (mm) at sugar cane field, 2022/2023 season, Rio Tinto, Paraíba, Brazil.

During the period from 1 October 2022 to 31 August 2023, 23 days had data gaps (15 of them in May 2023). The average tower-based daily evapotranspiration (ET) was 2.68 mm/day, considering only days without missing data, while the partial evapotranspiration, considering all times, was 883.4 mm. The highest daily totals occurred on 26 February 2023 (4.54 mm); 20 January 2023 (4.39 mm); and 25 January 2023 (4.22 mm). At the beginning of the sugarcane cycle and on dates with significant rainfall events, ET values were lower.

The accumulated precipitation during the period was 1520 mm, with a total of 175 days recording rainfall ($p > 0$ mm). The highest daily precipitation occurred on 9 June 2023, with 145.8 mm, followed by 7 July 2023 (96 mm), and 20 August 2023 (82 mm). June 2023 was the rainiest month, with 465.6 mm of rainfall, while the observed ET was 72.1 mm.

In contrast, November 2022 recorded no precipitation in the area, and the partial monthly ET (one day of missing data) was 68.3 mm. January 2023 had the highest ET, with 105.1 mm, and precipitation of 73.4 mm.

Figure 7 illustrates the main components of the surface energy balance, Rn, G, H, and LE. Net radiation represents the primary source of available energy in the system, which is mainly partitioned between LE and H; ground heat flux is negligible during most of the analyzed period.

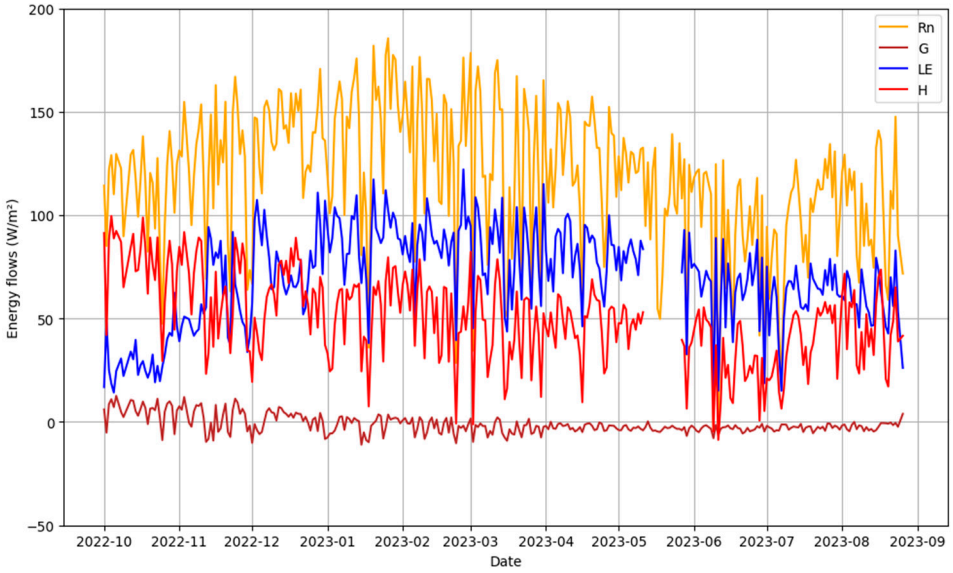

Figure 7. Components of energy balance over time.

The G/Rn ratio generally remained within the expected range, fluctuating between −1 and 1 throughout the study period (Figure 8).

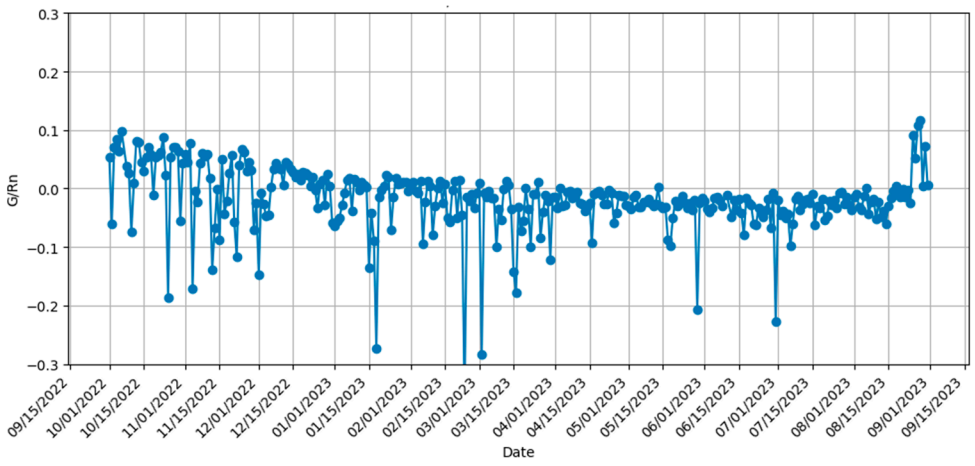

Figure 8. G/Rn ratio over time.

The predictive skill of QWaterModel in estimating Rn and G (Figures S2–S4 in Supplementary Materials) from surface temperature was assessed by comparing its estimates with tower-based data. The scatter plots in Figures 9 and 10 show a strong correlation between the model-estimated 30 min ***Rn*** and ***G*** and the tower-based data.

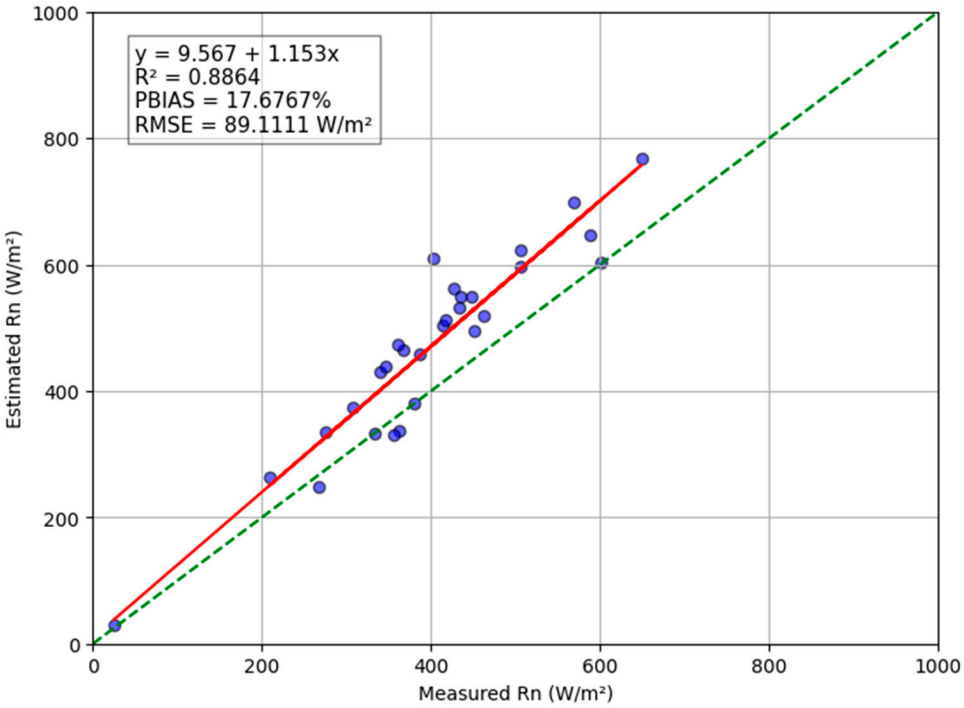

Figure 9. Comparison between estimated (QWater) and observed (tower-based) net radiation (Rn). The red solid line shows the fitted linear regression, and the green dashed line represents the 1:1 relationship.

The maximum difference (207 W/m^2) (Figure 9) between the modeled and observed Rn occurred on 17 November 2022, whereas the minimum difference (1 W/m^2) was found on 24 March 2023. The calculated root mean square error (RMSE) was 89.11 W/m^2. Regarding G, the largest difference occurred on 12 October 2022 (22.63 W/m^2), and the smallest on 18 August 2023 (0.0025 W/m^2), with an RMSE of only 8.03 W/m^2.

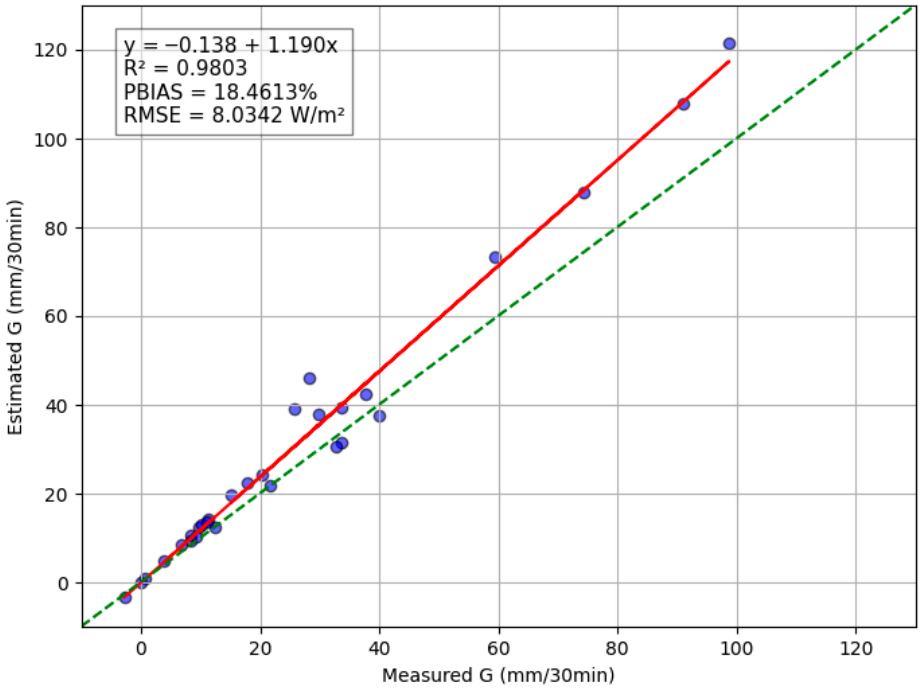

Figure 10. Comparison between estimated (QWater) and observed (tower-based) ground heat flux (G). The red solid line shows the fitted linear regression, and the green dashed line represents the 1:1 relationship.

Despite the accurate Rn and G estimates and good correlation between observed and modeled ET, QWater consistently overestimated 30 min ET (Figure 11). In the same figure, the PT-JPL model estimates can be compared with the flux tower values.

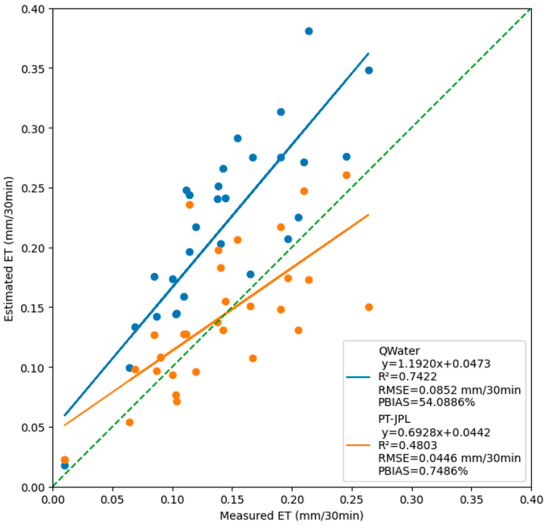

Figure 11. Comparison between tower-based ET and ET estimated by QWater-based (blue) and PT-JPL (orange). The fitted linear regressions for each model are shown as solid lines (blue for QWater and orange for PT-JPL), while the green dashed line represents the 1:1 relationship.

3.3. ET Partioning (PT-JPL)

Figures 12–15 shows ET modeled by PT-JPL, as well as the total half-hourly evapotranspiration on four analyzed dates, for each ET component: soil evaporation (ETs), canopy transpiration (ETc), and canopy interception (ETi). Ei was considered only for dates in which precipitation occurred in the previous 24 h and, therefore, disregarded for most dates. The Supplementary Materials list the orthomosaics in the remaining data (Figures S12–S36).

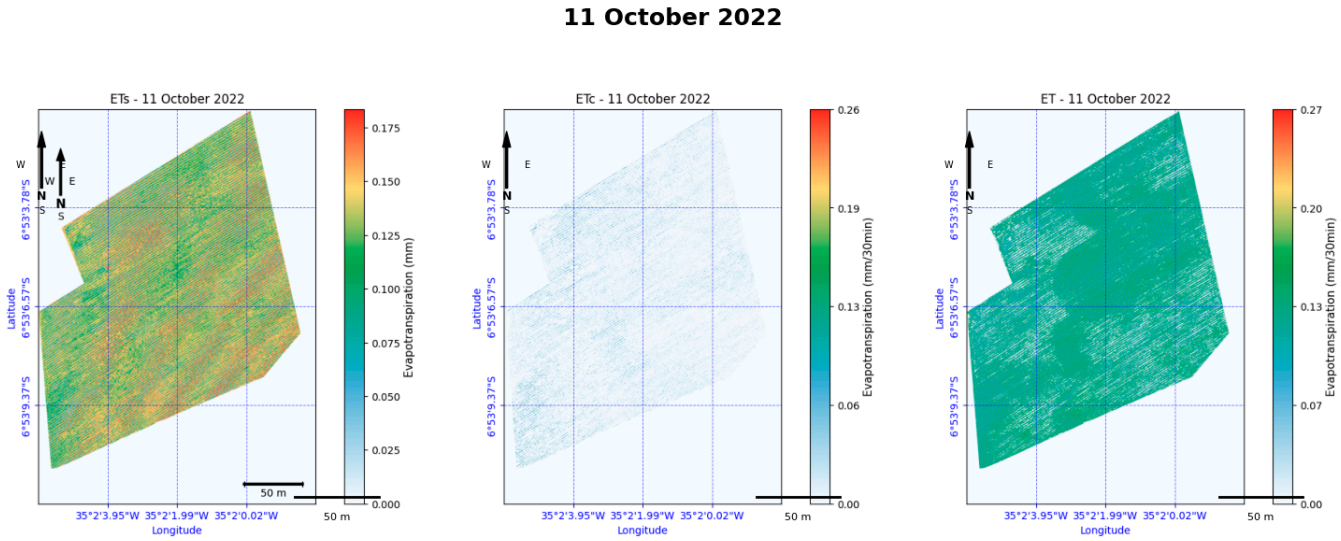

Figure 12. Spatial distribution of ET on 11 October 2022 (mm/30 min).

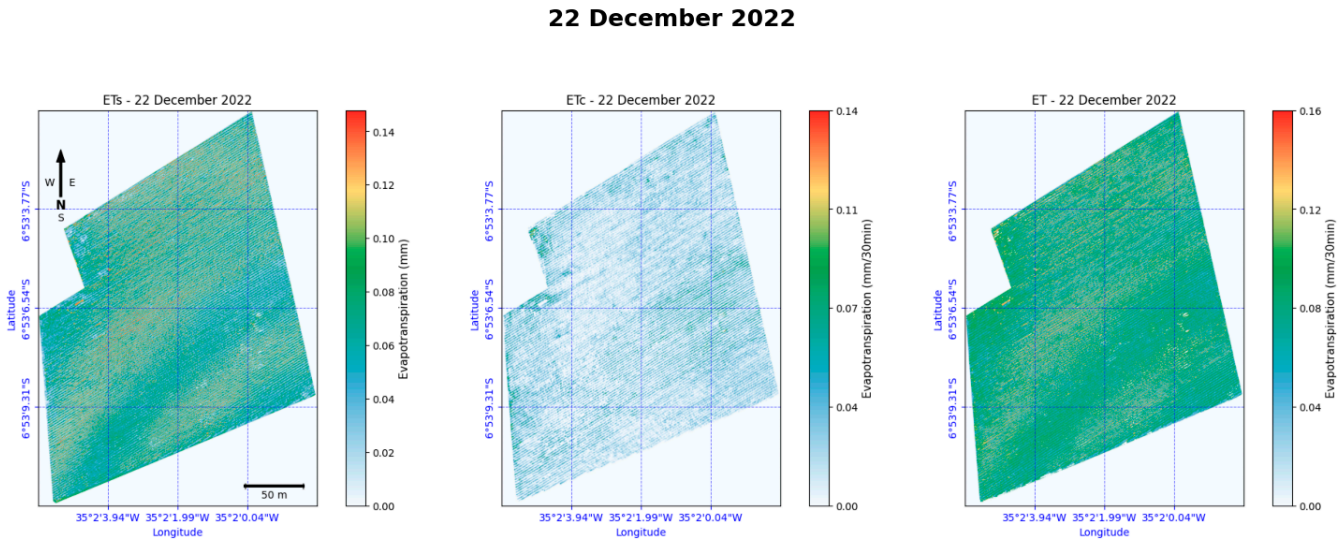

Figure 13. Spatial distribution of ET on 22 December 2022 (mm/30 min).

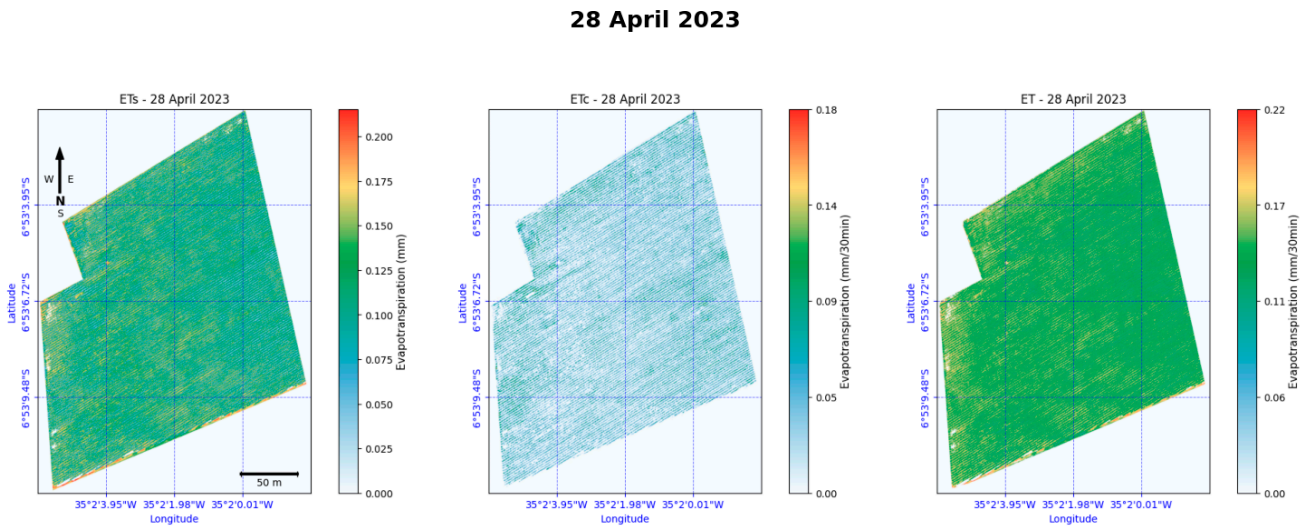

Figure 14. Spatial distribution of ET on 28 April 2023 (mm/30 min).

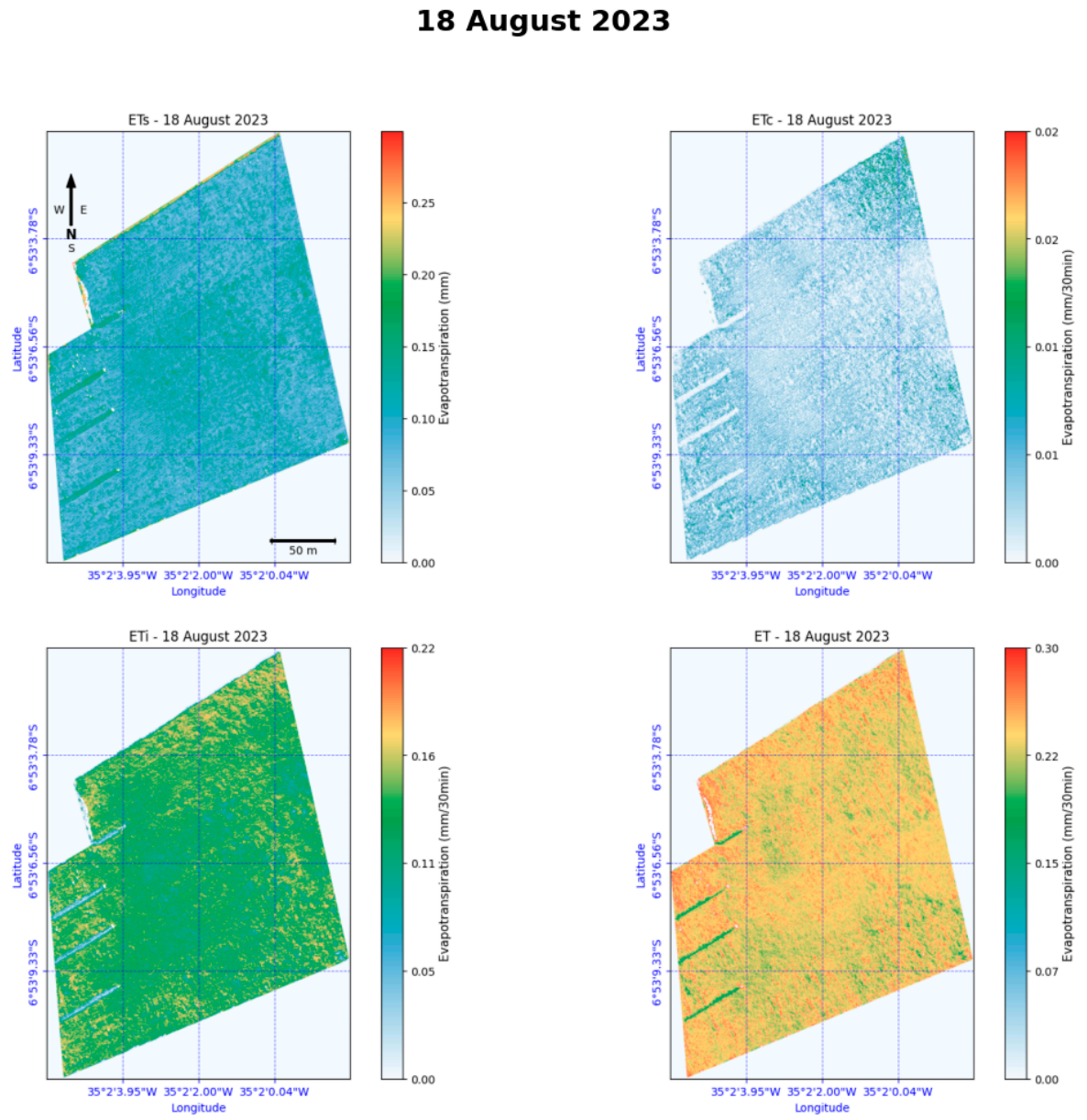

Figure 15. Spatial distribution of ET on 18 August 2023 (mm/30 min).

4. Discussion

Throughout the seasonal cycle of sugarcane cultivation (Figure 7), the components of the surface energy balance vary significantly depending on the plant's phenological stage. In the early stages of the sugarcane crop cycle, when vegetation cover is scarce, most of the net radiation reaches the soil surface, and the areas between planting rows exhibit a significantly higher surface temperature compared to the rest of the area. This scenario leads to a greater heat flux in the soil (G) and a higher proportion of energy converted into sensible heat (H) due to low evapotranspiration rates. This suggests that the microclimate is primarily driven by the physical properties of the soil, and not by plant physiological factors, making the crop more vulnerable to water loss due to heat.

During the first weeks after harvest (mid-September 2022), energy is primarily utilized for heating the air, as indicated by the relatively high H values in October 2022. Most of the available energy is converted into H due to the reduced leaf area and low transpiration rates characteristic of the initial growth stage. From November onwards, as the canopy develops, a shift in energy partitioning occurs: H gradually decreases while LE becomes

the dominant flux. This inversion reflects the plant's intensified physiological activity and the shift of the energy balance toward evapotranspiration.

Furthermore, higher G/Rn values can be observed because most of the net radiation is directed towards heating the soil. These values reflect the high thermal instability of the soil surface. This increase in G can lead to scenarios such as accelerated decomposition of organic matter and/or affect the germination/production rate. Therefore, the heterogeneous temperature values found from 26 May onwards may reflect these adverse scenarios and be related to growth or irrigation failures, or the occurrence of pests or diseases.

As the crop progresses and the sugarcane grows, forming a denser vegetation cover, the vegetation cover becomes more uniform, reducing the soil's exposure to direct solar radiation. Consequently, this leads to a more homogeneous surface temperature across the cultivated area. As there is an increase in radiation interception by the foliage, there is a reduction in heat flux in the soil, which promotes energy dissipation through latent heat (LE), associated with evapotranspiration. Consequently, a reduction in sensible heat is observed. The change caused by plant growth indicates the transition of the relevant components in the balance, previously dominated by soil evaporation and now dominated by plant transpiration. This indicates that the crop is moving toward a stage of maximum water use efficiency, in which energy is used for development rather than just heating the soil and surrounding air. In this scenario, the G/Rn ratio decreases, reaching minimum values in fully developed crops, which can be explained by the low incidence of radiation in the soil. After harvest or during senescence, the G/Rn ratio increases again.

It should be noted that, in addition to varying throughout the crop growth cycle, the G/Rn ratio also varies throughout the day. On a typical day, the G/Rn ratio is relatively low in the early morning, rises to temporary peaks during the period of maximum solar radiation, usually between 10 a.m. and 2 p.m., and decreases in the afternoon as soil temperature stabilizes and available energy is predominantly used for evapotranspiration.

The differences shown in Figure 9 can be influenced by several factors, mainly cloud cover and diffuse radiation. In the short term, cloud cover can change rapidly, consequently affecting the amount of direct and diffuse solar radiation reaching the surface, with an increase in diffuse radiation. The flux tower measures radiation every 10 s and calculates an average every half hour, capturing short-term variations that may not be reflected in the radiation balance estimated by the QWaterModel. This difference highlights the QWaterModel's sensitivity to radiation. This suggests that the model may present more suitable values on clear days; however, under conditions such as high humidity or cloudy skies, it may present discrepant values for LE flux, which is the main critical factor for irrigation management in semi-arid regions.

As defined by the developer, the QWaterModel estimates the radiation balance under clear-sky conditions, ignoring cloud-induced variations [36]. Rn is driven by the balance between incoming shortwave radiation, surface reflectance, and longwave radiation exchange between the surface and the atmosphere [44]. In addition, G is affected not only by radiation and surface temperature, but also by the temperature and thermal properties throughout the soil profile [45]. Although G accounts for only a small fraction of the surface energy balance relative to other components, it provides a right indication of the direction and magnitude of energy transfer between the soil and the atmosphere, making it a vital component of the surface energy balance and essential for understanding soil–atmosphere interactions. Its accurate measurement contributes significantly to the closure of the energy balance [46].

The temporal scaling of net radiation was performed using the ratio between flux measurements taken during the flight times and at the same time on the days without flight. This approach implicitly assumes that the spatial pattern of net radiation measured

by UAVs remains unchanged throughout the day, with only its magnitude varying over time. This assumption is generally valid under quasi-stationary atmospheric conditions, typically associated with clear skies and low spatial variability in cloud cover.

However, under more dynamic conditions, this assumption may be violated. Moving clouds can introduce spatially heterogeneous shading, altering the spatial distribution of net radiation. When conducting aerial surveys, it is imperative to acknowledge that data collection is not an instantaneous process. The flight over the area of interest necessitates a certain amount of time during which cloud conditions may change.

In scenarios characterized by clear skies or slowly varying cloud cover, the relationship between the fluxes measured at the tower and those observed during flight acquisitions tends to remain more consistent, enabling a more reliable temporal scaling. However, the presence of cloud cover at the research site is a notable variable, given its proximity to the coast. By applying the ratio of Rn or G during flight to the corresponding ratio at a time when no flight is occurring, it is possible to incorporate the prevailing atmospheric and ground conditions into this correction. It is possible to satisfactorily complete the ET series in agricultural settings by applying extrapolations based solely on global radiation data [41]. Using Rn as the reference variable, the results of the extrapolation from ET are accurate; therefore, the applicability of the method depends on the temporal proximity between measurements [40].

The DATTUTDUT model, the original model from which QWaterModel is based, performed well when validated against eddy covariance measurements over grasslands in Germany [47]. It also showed good results in two studies conducted in oil palm plantations in Sumatra, Indonesia [36,48]. However, these findings contrast with those of [49], who observed low agreement with field measurements in an area cultivated with maize and fennel in southern Italy [49].

Figure 11 shows the comparison between evapotranspiration calculated by the energy balance method and that estimated by QWaterModel. For ET, the RMSE of 0.08 mm/30 min indicates good performance in terms of mean error, although the lower R^2 (0.72) suggests the model has a reduced ability to capture data variability compared to radiation. These results suggest that the model is better adjusted for radiation, whereas for ET, it maintains mean values close to observed values but explains less variability.

According to [50], the PT-JPL model assumes that Ei occurs when relative humidity (RH) reaches 70%, which is not always true, as even high RH does not necessarily result in precipitation or dew formation. Another factor contributing to a null or negligible Ei is the absence of significant rainfall, resulting in a lack of intercepted water on the canopy surface. Reference [51] highlights that two other factors affecting Ei in cultivated areas are irrigation intensity and crop density. According to the authors, an increase in ETc is generally accompanied by a reduction in ETi.

The mechanisms governing the individual components of evapotranspiration in the PT-JPL model operate at different spatial and temporal scales [52]. In the early stages of the crop growth cycle, soil evaporation is the primary contributor to ET, influenced by atmospheric evaporative demand and soil moisture [53]. Plant transpiration and canopy interception are relatively low at this stage, as both biomass and leaf area are small. Leaf Area Index (LAI), a key parameter describing vegetation characteristics, is a major factor affecting ET partitioning, as LAI increases, canopy transpiration rises and soil evaporation decreases [42].

The results presented in Figure 11 indicate that the simulated values oscillate closely around the observations, which, associated with the low PBIAS (absence of systematic bias), suggests that the model provides a consistent and reliable estimation of evapotranspiration

over the analyzed timeframe. This value is lower than that reported by [54], who reported $R^2 = 0.70$ and $R^2 = 0.62$ at two different locations.

The PT-JPL model underestimated evapotranspiration, with the underestimation more pronounced when shortwave radiation in the QWaterModel was higher. The underestimation on days with high shortwave radiation is attributable to a combination of model simplifications and the actual responses of vegetation and soil, which can be more sensitive to radiation than the PT-JPL model predicts.

Overall, the results demonstrate that the PT-JPL model, driven by ultra-high spatial resolution imagery acquired via UAV, can capture the main patterns of evapotranspiration in sugarcane fields and provide reliable estimates under varying meteorological and phenological conditions. Although some underestimation was observed under high shortwave radiation, the model maintained satisfactory accuracy and consistency relative to flux tower data. These findings reinforce the potential of PT-JPL for operational applications in large-scale or data-limited agricultural monitoring, particularly when coupled with other remote-sensing approaches, such as the QWaterModel. Nevertheless, further improvements—especially in the representation of irrigation, canopy structure, and soil moisture variability—are necessary to enhance its predictive performance and to ensure better applicability across different climatic and management conditions.

Monitoring and measuring terrestrial evaporation are essential for several fields. This topic has been a constant focus of research over recent decades, driven by unresolved issues. Advances in observational techniques and our understanding of ET dynamics offer new opportunities for deeper comprehension and a more accurate description of the processes involved in the ET phenomenon [30]. Accurate detection of the spatial and temporal variations in ET is crucial for understanding the water cycle and surface energy balance, especially in the context of climate change [29].

In addition to climate-related uncertainties, several other issues remain unresolved in the study of terrestrial evaporation and evapotranspiration. These include the representation of irrigation and agricultural practices in models, as well as the influence of spatial heterogeneity in soil, vegetation, and topography. Furthermore, challenges persist in capturing the interactions between radiation, soil moisture, and vegetation response under water stress, as well as in reconciling ground-based and satellite-derived ET estimates across spatial and temporal scales. Addressing these knowledge gaps is essential for improving the accuracy and transferability of ET models under diverse climatic and land-use conditions.

However, some limitations remain. The PT-JPL model does not fully account for irrigation practices or for detailed canopy structural variations, both of which can influence ET estimates. Additionally, factors such as cloud dynamics, atmospheric variability, and soil heterogeneity may introduce uncertainties into the models. Future research should focus on incorporating irrigation parameters, improving the representation of vegetation structure, and integrating soil moisture dynamics to refine ET predictions.

Overall, this study highlights the viability of combining UAV-derived data with physically based modeling approaches for accurate, spatially explicit estimation of evapotranspiration. Such advances significantly improve irrigation management, optimize water resource use, and promote sustainable agricultural practices in tropical and semi-arid environments.

5. Conclusions

Radiometric temperature calibration proved effective in improving the accuracy of surface temperature estimation. The use of micrometeorological data was essential for estimating ET. Accurate ET estimation is crucial, as it enables the optimization of water

resource use, improves agricultural management efficiency, and increases crop productivity. The installation of additional flux towers, similar to rainfall monitoring networks, could provide Supplementary Data.

The calibration of radiometric temperature and the validation of models highlight the importance of an integrated approach to evapotranspiration estimation, with potential to enhance water resource management and agricultural productivity. Understanding and accurately estimating evapotranspiration enables the optimization of water resource use, improves agricultural management efficiency, and increases crop productivity. Given the growing importance of sustainable agriculture, the ability to measure and monitor evapotranspiration is increasingly relevant to food security and natural resources conservation.

The integration of UAV-based thermal and multispectral imagery with evapotranspiration models proved effective for estimating and mapping ET in sugarcane cultivation areas in Northeast Brazil. The results demonstrated strong agreement between modeled and observed data, with both the QWaterModel and PT-JPL performing consistently under tropical agricultural conditions. The QWaterModel provided accurate estimates of surface energy fluxes, especially for net radiation and soil heat flux, while the PT-JPL model effectively captured the spatial distribution and temporal dynamics of ET, despite a slight tendency to underestimate values under high shortwave radiation.

The study reinforces the potential of using UAVs as complementary tools for field-based ET monitoring, providing high-resolution data that enhance the spatial representation of surface energy balance components. The ability to integrate these datasets with free or open-source models such as PT-JPL and QWaterModel offers a promising pathway for operational water management, particularly in regions with limited access to satellite data or frequent cloud cover.

Supplementary Materials: The following supporting information can be downloaded at: https://www.mdpi.com/article/10.3390/agriengineering8040149/s1, Figure S1: Surface temperature maps (°C); Figure S2: Spatial distribution of Rn and G (part 1); Figure S3: Spatial distribution of Rn and G (part 2); Figure S4: Spatial distribution of Rn and G (part 3); Figure S5: Spatial distribution of Rn and G (part 4); Figure S6: Spatial distribution of Rn and G (part 5); Figure S7: Spatial distribution of Rn and G (part 6); Figure S8: Spatial distribution of Rn and G (part 7); Figure S9: Spatial distribution of Rn and G (part 8); Figure S10: Spatial distribution of Rn and G (part 9); Figure S11: Spatial distribution of Rn and G (part 10); Figure S12: Spatial distribution of ET on 10 October 2022; Figure S13: Spatial distribution of ET on 12 October 2022; Figure S14: Spatial distribution of ET on 3 November 2022; Figure S15: Spatial distribution of ET on 4 November 2022; Figure S16: Spatial distribution of ET on 5 November 2022; Figure S17: Spatial distribution of ET on 15 November 2022; Figure S18: Spatial distribution of ET on 16 November 2022; Figure S19: Spatial distribution of ET on 17 November 2022; Figure S20: Spatial distribution of ET on 24 November 2022; Figure S21: Spatial distribution of ET on 25 November 2022; Figure S22: Spatial distribution of ET on 26 November 2022; Figure S23: Spatial distribution of ET on 21 December 2022; Figure S24: Spatial distribution of ET on 23 December 2022; Figure S25: Spatial distribution of ET on 23 March 2023; Figure S26: Spatial distribution of ET on 24 March 2023; Figure S27: Spatial distribution of ET on 25 March 2023; Figure S28: Spatial distribution of ET on 27 April 2023; Figure S29: Spatial distribution of ET on 29 April 2023; Figure S30: Spatial distribution of ET on 26 May 2023; Figure S31: Spatial distribution of ET on 27 May 2023; Figure S32: Spatial distribution of ET on 20 July 2023; Figure S33: Spatial distribution of ET on 21 July 2023; Figure S34: Spatial distribution of ET on 22 July 2023; Figure S35: Spatial distribution of ET on 17 August 2023; Figure S36: Spatial distribution of ET on 19 August 2023.

Author Contributions: Conceptualization, D.d.C.D.M. and V.P.B.; methodology, D.d.C.D.M. and L.A.d.C.J.; software, É.R.O.C. and A.F.d.N.; investigation, E.A.C.; validation, M.E.d.O.J. and D.d.C.D.M.; formal analysis, D.d.C.D.M., V.P.B. and M.E.d.O.J.; resources, G.F.B. and E.W.; data curation, V.P.B.; writing—original draft preparation, M.E.d.O.J.; writing—review and editing, D.d.C.D.M.,

L.A.d.C.J., V.P.B. and G.F.B.; project administration, D.d.C.D.M.; funding acquisition, E.W. and D.d.C.D.M. All authors have read and agreed to the published version of the manuscript.

Funding: This research was funded by FAPESQ—Fundação de Apoio à Pesquisa da Paraíba (Paraíba State Research Foundation) grant number 262/2020; and São Paulo Research Foundation (FAPESP): grant 2019/23946-3.

Institutional Review Board Statement: Not applicable.

Informed Consent Statement: Not applicable.

Data Availability Statement: Dataset available on request from the authors.

Acknowledgments: Computational infrastructure for aerial image processing was kindly provided by the Open-Lab DREAM (RITM-BFC).

Conflicts of Interest: Lúcio André de Castro Jorge was employed by the Brazilian Agricultural Research Corporation. The remaining authors declare that the research was conducted in the absence of any commercial or financial relationships that could be construed as a potential conflict of interest.

References

1. Young, G.; Demuth, S.; Mishra, A.; Cudennec, C. Hydrological Sciences and Water Security: An Overview. *Proc. Int. Assoc. Hydrol. Sci.* **2015**, *366*, 1–9. [CrossRef]
2. Chang, F.-J.; Guo, S. Advances in Hydrologic Forecasts and Water Resources Management. *Water* **2020**, *12*, 1819. [CrossRef]
3. Nannawo, A.S.; Lohani, T.K.; Eshete, A.A. Exemplifying the Effects Using WetSpass Model Depicting the Landscape Modifications on Long-Term Surface and Subsurface Hydrological Water Balance in Bilate Basin, Ethiopia. *Adv. Civ. Eng.* **2021**, *2021*, 7283002. [CrossRef]
4. Jiang, X.; Wang, Y.; Yinglan, A.; Wang, G.; Zhang, X.; Ma, G.; Duan, L.; Liu, K. Optimizing Actual Evapotranspiration Simulation to Identify Evapotranspiration Partitioning Variations: A Fusion of Physical Processes and Machine Learning Techniques. *Agric. Water Manag.* **2024**, *295*, 108755. [CrossRef]
5. Wanniarachchi, S.; Sarukkalige, R. A Review on Evapotranspiration Estimation in Agricultural Water Management: Past, Present, and Future. *Hydrology* **2022**, *9*, 123. [CrossRef]
6. Liu, S.; Xu, Z. Micrometeorological Methods to Determine Evapotranspiration. In *Observation and Measurement*; Li, X., Vereecken, H., Eds.; Ecohydrology; Springer: Berlin/Heidelberg, Germany, 2018; pp. 1–39, ISBN 978-3-662-47871-4.
7. Moorhead, J.E.; Marek, G.W.; Gowda, P.H.; Lin, X.; Colaizzi, P.D.; Evett, S.R.; Kutikoff, S. Evaluation of Evapotranspiration from Eddy Covariance Using Large Weighing Lysimeters. *Agronomy* **2019**, *9*, 99. [CrossRef]
8. Fong, T.Y.; Huang, Y.F.; Chin, R.J.; Koo, C.H. Advancing Evapotranspiration Estimation with Remote Sensing and Artificial Intelligence—A Review. *Agric. Water Manag.* **2025**, *322*, 110023. [CrossRef]
9. Rana, G.; Katerji, N. Measurement and Estimation of Actual Evapotranspiration in the Field under Mediterranean Climate: A Review. *Eur. J. Agron.* **2000**, *13*, 125–153. [CrossRef]
10. Pinos, J. Estimation Methods to Define Reference Evapotranspiration: A Comparative Perspective. *Water Pract. Technol.* **2022**, *17*, 940–948. [CrossRef]
11. Zhang, K.; Kimball, J.S.; Running, S.W. A Review of Remote Sensing Based Actual Evapotranspiration Estimation. *WIREs Water* **2016**, *3*, 834–853. [CrossRef]
12. Zhao, L.; Xia, J.; Xu, C.; Wang, Z.; Sobkowiak, L.; Long, C. Evapotranspiration Estimation Methods in Hydrological Models. *J. Geogr. Sci.* **2013**, *23*, 359–369. [CrossRef]
13. Ezenne, G.I.; Eyibio, N.U.; Tanner, J.L.; Asoiro, F.U.; Obalum, S.E. An Overview of Uncertainties in Evapotranspiration Estimation Techniques. *J. Agrometeorol.* **2023**, *25*, 173–182. [CrossRef]
14. Enku, T.; Melesse, A.M. A Simple Temperature Method for the Estimation of Evapotranspiration. *Hydrol. Process.* **2014**, *28*, 2945–2960. [CrossRef]
15. Bambach, N.; Kustas, W.; Alfieri, J.; Prueger, J.; Hipps, L.; McKee, L.; Castro, S.J.; Volk, J.; Alsina, M.M.; McElrone, A.J. Evapotranspiration Uncertainty at Micrometeorological Scales: The Impact of the Eddy Covariance Energy Imbalance and Correction Methods. *Irrig. Sci.* **2022**, *40*, 445–461. [CrossRef]
16. Callejas-Rodelas, J.Á.; Knohl, A.; Mammarella, I.; Vesala, T.; Peltola, O.; Markwitz, C. Does Increased Spatial Replication above Heterogeneous Agroforestry Improve the Representativeness of Eddy Covariance Measurements? *Biogeosciences* **2025**, *22*, 4507–4529. [CrossRef]

17. Chu, H.; Luo, X.; Ouyang, Z.; Chan, W.S.; Dengel, S.; Biraud, S.C.; Torn, M.S.; Metzger, S.; Kumar, J.; Arain, M.A.; et al. Representativeness of Eddy-Covariance Flux Footprints for Areas Surrounding AmeriFlux Sites. *Agric. For. Meteorol.* **2021**, *301–302*, 108350. [CrossRef]
18. Griebel, A.; Bennett, L.T.; Metzen, D.; Cleverly, J.; Burba, G.; Arndt, S.K. Effects of Inhomogeneities within the Flux Footprint on the Interpretation of Seasonal, Annual, and Interannual Ecosystem Carbon Exchange. *Agric. For. Meteorol.* **2016**, *221*, 50–60. [CrossRef]
19. Liu, X.; Xu, J.; Zhou, X.; Wang, W.; Yang, S. Evaporative Fraction and Its Application in Estimating Daily Evapotranspiration of Water-Saving Irrigated Rice Field. *J. Hydrol.* **2020**, *584*, 124317. [CrossRef]
20. Buttar, N.A.; Hu, Y.; Tanny, J.; Raza, A.; Niaz, Y.; Khan, M.I.; Saddique, N.; Sarwar, A.; Azeem, A.; Ahmed, F.; et al. Estimation of Sensible and Latent Heat Fluxes Using Flux Variance Method under Unstable Conditions: A Case Study of Tea Plants. *Atmosphere* **2022**, *13*, 1545. [CrossRef]
21. Fisher, J.B.; Tu, K.P.; Baldocchi, D.D. Global Estimates of the Land–Atmosphere Water Flux Based on Monthly AVHRR and ISLSCP-II Data, Validated at 16 FLUXNET Sites. *Remote Sens. Environ.* **2008**, *112*, 901–919. [CrossRef]
22. Som-ard, J.; Atzberger, C.; Izquierdo-Verdiguier, E.; Vuolo, F.; Immitzer, M. Remote Sensing Applications in Sugarcane Cultivation: A Review. *Remote Sens.* **2021**, *13*, 4040. [CrossRef]
23. Zheng, Y.; dos Santos Luciano, A.C.; Dong, J.; Yuan, W. High-Resolution Map of Sugarcane Cultivation in Brazil Using a Phenology-Based Method. *Earth Syst. Sci. Data* **2022**, *14*, 2065–2080. [CrossRef]
24. Resende, R.S.; Nascimento, T.; de Carvalho, T.B.; Amorim, J.R.A.; Rodrigues, L. Reducing Sugarcane Irrigation Demand through Planting Date Adjustment in Alagoas State, Brazil. *Rev. Bras. Eng. Agríc. Ambient.* **2021**, *25*, 75–81. [CrossRef]
25. Araújo Palharini, R.S.; Vila, D.A. Climatological Behavior of Precipitating Clouds in the Northeast Region of Brazil. *Adv. Meteorol.* **2017**, *2017*, 5916150. [CrossRef]
26. Ruwanpathirana, P.P.; Sakai, K.; Jayasinghe, G.Y.; Nakandakari, T.; Yuge, K.; Wijekoon, W.M.C.J.; Priyankara, A.C.P.; Samaraweera, M.D.S.; Madushanka, P.L.A. Evaluation of Sugarcane Crop Growth Monitoring Using Vegetation Indices Derived from RGB-Based UAV Images and Machine Learning Models. *Agronomy* **2024**, *14*, 2059. [CrossRef]
27. de Lima, G.S.A.; Ferreira, M.E.; Sales, J.C.; de Souza Passos, J.; Maggiotto, S.R.; Madari, B.E.; de Melo Carvalho, M.T.; de Almeida Machado, P.L.O. Evapotranspiration Measurements in Pasture, Crops, and Native Brazilian Cerrado Based on UAV-Borne Multispectral Sensor. *Environ. Monit. Assess.* **2024**, *196*, 1105. [CrossRef] [PubMed]
28. Wei, J.; Sun, J.; Liu, S.; Song, L.; Ma, Y.; Xu, Z.; Xu, T.; Zhou, J.; Wang, Z.; Peng, Z.; et al. A Robust Framework for Improving Fine-Scale Evapotranspiration Estimation From UAV-Based Multispectral and Thermal Images. *IEEE Trans. Geosci. Remote Sens.* **2025**, *63*, 4417615. [CrossRef]
29. Fu, J.; Wang, W.; Shao, Q.; Xing, W.; Cao, M.; Wei, J.; Chen, Z.; Nie, W. Improved Global Evapotranspiration Estimates Using Proportionality Hypothesis-Based Water Balance Constraints. *Remote Sens. Environ.* **2022**, *279*, 113140. [CrossRef]
30. McCabe, M.F.; Miralles, D.G.; Holmes, T.R.H.; Fisher, J.B. Advances in the Remote Sensing of Terrestrial Evaporation. *Remote Sens.* **2019**, *11*, 1138. [CrossRef]
31. Becker, C.T.; Bandeira, M.M. Atlas Pluviométrico Da Paraíba. Available online: http://www.aesa.pb.gov.br/biblioteca/atlas-pluviometrico-da-paraiba/ (accessed on 28 October 2025).
32. Martínez-Carricondo, P.; Agüera-Vega, F.; Carvajal-Ramírez, F.; Mesas-Carrascosa, F.-J.; García-Ferrer, A.; Pérez-Porras, F.-J. Assessment of UAV-Photogrammetric Mapping Accuracy Based on Variation of Ground Control Points. *Int. J. Appl. Earth Obs. Geoinf.* **2018**, *72*, 1–10. [CrossRef]
33. Kelly, J.; Kljun, N.; Olsson, P.-O.; Mihai, L.; Liljeblad, B.; Weslien, P.; Klemedtsson, L.; Eklundh, L. Challenges and Best Practices for Deriving Temperature Data from an Uncalibrated UAV Thermal Infrared Camera. *Remote Sens.* **2019**, *11*, 567. [CrossRef]
34. Rodríguez, M.V.; Melgar, S.G.; Márquez, J.M.A. Assessment of Aerial Thermography as a Method of in Situ Measurement of Radiant Heat Transfer in Urban Public Spaces. *Sustain. Cities Soc.* **2022**, *87*, 104228. [CrossRef]
35. Mahmoud, A.A.E.; Attaher, S.M.; Snyder, R.L. Evaluation of Surface Renewal VS. Eddy Covariance Methods to Estimate Cereal Crops Evapotranspiration. *J. Soil Sci. Agric. Eng.* **2020**, *11*, 845–851. [CrossRef]
36. Ellsäßer, F.; Röll, A.; Stiegler, C.; Hendrayanto; Hölscher, D. Introducing QWaterModel, a QGIS Plugin for Predicting Evapotranspiration from Land Surface Temperatures. *Environ. Model. Softw.* **2020**, *130*, 104739. [CrossRef]
37. Timmermans, W.J.; Kustas, W.P.; Andreu, A. Utility of an Automated Thermal-Based Approach for Monitoring Evapotranspiration. *Acta Geophys.* **2015**, *63*, 1571–1608. [CrossRef]
38. Schuurmans, J.M.; Troch, P.A.; Veldhuizen, A.A.; Bastiaanssen, W.G.M.; Bierkens, M.F.P. Assimilation of Remotely Sensed Latent Heat Flux in a Distributed Hydrological Model. *Adv. Water Resour.* **2003**, *26*, 151–159. [CrossRef]
39. Hoch, S.W.; Whiteman, C.D. Topographic Effects on the Surface Radiation Balance in and around Arizona's Meteor Crater. *J. Appl. Meteorol. Climatol.* **2010**, *49*, 1114–1128. [CrossRef]
40. Alfieri, J.G.; Anderson, M.C.; Kustas, W.P.; Cammalleri, C. Effect of the Revisit Interval and Temporal Upscaling Methods on the Accuracy of Remotely Sensed Evapotranspiration Estimates. *Hydrol. Earth Syst. Sci.* **2017**, *21*, 83–98. [CrossRef]

41. Delogu, E.; Olioso, A.; Alliès, A.; Demarty, J.; Boulet, G. Evaluation of Multiple Methods for the Production of Continuous Evapotranspiration Estimates from TIR Remote Sensing. *Remote Sens.* **2021**, *13*, 1086. [CrossRef]
42. Zhang, L.; Marshall, M.; Nelson, A.; Vrieling, A. A Global Assessment of PT-JPL Soil Evaporation in Agroecosystems with Optical, Thermal, and Microwave Satellite Data. *Agric. For. Meteorol.* **2021**, *306*, 108455. [CrossRef]
43. Athira, K.V.; Eswar, R.; Boulet, G.; Nigam, R.; Bhattacharya, B.K. Modeling Evapotranspiration at Larger Temporal Scales: Effects of Temporal Aggregation and Data Gaps. *Remote Sens.* **2022**, *14*, 4142. [CrossRef]
44. Xie, T.; Li, J.; Yang, C.; Jiang, Z.; Chen, Y.; Guo, L.; Zhang, J. Crop Height Estimation Based on UAV Images: Methods, Errors, and Strategies. *Comput. Electron. Agric.* **2021**, *185*, 106155. [CrossRef]
45. An, K.; Wang, W.; Wang, Z.; Zhao, Y.; Yang, Z.; Chen, L.; Zhang, Z.; Duan, L. Estimation of Ground Heat Flux from Soil Temperature over a Bare Soil. *Theor. Appl. Climatol.* **2017**, *129*, 913–922. [CrossRef]
46. Wang, L.; Huang, M.; Qian, X.; Liu, L.; You, W.; Zhang, J.; Wang, M.; Che, R. Confined Magnetic-Dielectric Balance Boosted Electromagnetic Wave Absorption. *Small* **2021**, *17*, 2100970. [CrossRef] [PubMed]
47. Brenner, C.; Zeeman, M.; Bernhardt, M.; Schulz, K. Estimation of Evapotranspiration of Temperate Grassland Based on High-Resolution Thermal and Visible Range Imagery from Unmanned Aerial Systems. *Int. J. Remote Sens.* **2018**, *39*, 5141–5174. [CrossRef]
48. Ellsäßer, F.; Stiegler, C.; Röll, A.; June, T.; Hendrayanto; Knohl, A.; Hölscher, D. Predicting Evapotranspiration from Drone-Based Thermography—A Method Comparison in a Tropical Oil Palm Plantation. *Biogeosciences* **2021**, *18*, 861–872. [CrossRef]
49. Nisa, Z.; Khan, M.S.; Govind, A.; Marchetti, M.; Lasserre, B.; Magliulo, E.; Manco, A. Evaluation of SEBS, METRIC-EEFlux, and QWaterModel Actual Evapotranspiration for a Mediterranean Cropping System in Southern Italy. *Agronomy* **2021**, *11*, 345. [CrossRef]
50. Bai, P. Comparison of Remote Sensing Evapotranspiration Models: Consistency, Merits, and Pitfalls. *J. Hydrol.* **2023**, *617*, 128856. [CrossRef]
51. Nguyen, M.N.; Hao, Y.; Baik, J.; Choi, M. Partitioning Evapotranspiration Based on the Total Ecosystem Conductance Fractions of Soil, Interception, and Canopy in Different Biomes. *J. Hydrol.* **2021**, *603*, 126970. [CrossRef]
52. Talsma, C.J.; Good, S.P.; Jimenez, C.; Martens, B.; Fisher, J.B.; Miralles, D.G.; McCabe, M.F.; Purdy, A.J. Partitioning of Evapotranspiration in Remote Sensing-Based Models. *Agric. For. Meteorol.* **2018**, *260–261*, 131–143. [CrossRef]
53. Jiang, S.; Liang, C.; Zhao, L.; Gong, D.; Huang, Y.; Xing, L.; Zhu, S.; Feng, Y.; Guo, L.; Cui, N. Energy and Evapotranspiration Partitioning over a Humid Region Orchard: Field Measurements and Partitioning Model Comparisons. *J. Hydrol.* **2022**, *610*, 127890. [CrossRef]
54. Javadian, M.; Aubrecht, D.M.; Fisher, J.B.; Scott, R.L.; Burns, S.P.; Diehl, J.L.; Munger, J.W.; Richardson, A.D. Scaling Individual Tree Transpiration With Thermal Cameras Reveals Interspecies Differences to Drought Vulnerability. *Geophys. Res. Lett.* **2024**, *51*, e2024GL111479. [CrossRef]